Experimental Observation of Enhanced Radio-Frequency Sensors based on Self-Dual Emitter-Absorber

Minye Yang[1], Zhilu Ye[1], Mohamed Farhat[2], and Pai-Yen Chen[1, *]

[1]*Department of Electrical and Computer Engineering, University of Illinois at Chicago, Chicago, IL 60607, United States*

[2]*Computer, Electrical, and Mathematical Science and Engineering Division, King Abdullah University of Science and Technology (KAUST), Thuwal 23955-6900, Saudi Arabia*

Corresponding Author: Email: pychen@uic.edu

Abstract

We propose and experimentally demonstrate a parity-time (PT)-symmetric electronic system exhibiting the self-dual emitter-absorber property with a remarkable modulation depth in the radio-frequency (RF) region. The dramatically different RF responses between the emitter and absorber modes may allow detection of ultrasmall conductive or reactive perturbations. Our measurement results show that even a perturbation of the 10^{-2} order can greatly change the system's output intensity by more than 30 dB, consistent with the theoretical prediction. The measured sensitivity is far beyond traditional sensors based on a Fabry-Perot resonator, and may lead to monotonic RF sensors with high sensitivity and resolvability.

In the past decade, non-Hermitian physics, exemplified by parity-time (*PT*)-symmetry, has gained tremendous attention in the fields of quantum mechanics [1], optics, photonics [2–9], acoustics [10,11], and electronics [12–17]. These physical systems share a common feature, that is, the non-Hermitian degeneracy and exceptional points (EPs) where Taylor series expansion fails to converge in the multi-valued complex eigenspectrum. The appearance of branching singularities at EPs [7–9,18] has led to a variety of sensing [17–25], imaging [26,27], information processing [28–34], and wireless power transfer [35,36] applications. Besides, another unusual kind of singularity, coherent perfect absorber-laser (CPAL) point, can be observed in *PT*-symmetric systems [6,37–42] constituted by coupled gain and loss oscillators. Traditionally, a laser oscillator emits coherent outgoing radiations, while a CPA is a dark medium absorbing all incoming radiations (i.e., the time-reversed counterpart of a laser). However, at the CPAL point of *PT*-symmetric systems, the laser and CPA modes, which exhibit completely different scattering properties, can be switched at will through adjustment of the initial phase difference of two counter-propagating monotonic input waves. Experimental observations of such a self-dual singularity have been reported in optics and photonics [6,38], which show great promise for building the next-generation optical switches and interferometers [6,37–42].

Sensing may be one of the most interesting applications of non-Hermitian devices with exotic spectral singularities. Several groups have demonstrated that singular points in the *PT*-symmetric systems, such as EPs that cause the eigenvalue bifurcation effect, can be exploited to boost the resonance frequency shift and thus sensitivity of the RF or optical sensors [17–24]. However, it has been reported that EP-based sensors could be rather vulnerable to phase and flicker noises, as well as modal interference occurring near the higher-order EP [43–45], and could result in low spectrum/bandwidth efficiency, especially in the radio wave region. Very recently, we have theoretically proposed a monotonic (or monochromatic) optical sensor operating at the CPAL point for mitigating the noise and spectral efficiency issues observed in the EP-based

sensors [43–46]. Different from the EP-based sensors that monitor the shift of resonant peaks due to the eigenvalue bifurcation, the CPAL-sensor adopts a monotonic sensing scheme and detects the output intensity as a function of the impedance perturbation at a given frequency [46]. In this Letter, we further perform the first experimental demonstration of the CPAL-based *PT*-symmetric sensors with unprecedented sensitivity in the radio-frequency (RF) range.

Figures 1(a) and 1(b) present the schematics and circuit diagram of the proposed *PT*-symmetric RF sensor, which consists of a lossy component with a conductance G and an amplifying component with an effective negative conductance $-G$ (e.g., a negative impedance converter or NIC). These gain and loss elements are separated by an electrical length $x=\pi/2+\delta x,$ which can be realized with a transmission line segment or a compact T/Π equivalent circuit [Fig. 1(b)]. In order to achieve the CPAL effect, the conductance values must be tuned to: $G=|-G|=\sqrt{2}Y_0$, where Y_0 is the characteristic admittance of the transmission line segment [46]. The scattering matrix **S** can be used to connect the input and output voltage signals in the left ($-$) and right (+) ports: $|\psi_{\text{out}}\rangle=\mathbf{S}|\psi_{\text{in}}\rangle$, where $|\psi_{\text{in}}\rangle=(\psi_f^-,\psi_b^+)^T$ and $|\psi_{\text{out}}\rangle=(\psi_b^-,\psi_f^+)^T$ [Fig. 1(a)]. At the CPAL frequency (ω_0), the two eigenvalues of **S** ($\lambda_\pm$) would diverge into zero (i.e., CPA mode) and infinity (i.e., laser mode); see Appendix A1. Such a self-dual spectral singularity can be seen in Fig. 2(a) where $\delta x=10^{-2}\pi/2$. When a small impedance perturbation δY is introduced, this electronic *PT* system could be switched from the CPA mode to the laser mode and vice versa, resulting in a dramatic change in the output intensity. This property can be exploited to build new types of RF and microwave sensors with ultrahigh sensitivity. The laser and CPA modes can be characterized by the output coefficient Θ, defined as the ratio of the total output power to the total input power:

$$\Theta=\frac{|\psi_b^-|^2+|\psi_f^+|^2}{|\psi_f^-|^2+|\psi_b^+|^2}. \quad (1)$$

When the voltage ratio of two input waves $\psi_b^+/\psi_f^- = i(\sqrt{2}-1)$, the CPA mode ($\Theta \approx 0$) can be achieved, while the emitter mode is obtained at any other ψ_b^+/ψ_f^-. Let's first consider the conductive (resistive) sensing scenario, where the electronic circuit in Fig. 1(b) initially works at the CPA mode and a small conductive perturbation δG is introduced to the loss side. The output coefficient as a function of the conductive perturbation and the intentional phase offset δx can be approximately expressed as:

$$\Theta_{PT} \approx \frac{1}{4}\left[(\delta x)^2+\frac{\nu^2}{(\delta x)^2}\right]+\mathrm{O}(\nu^3), \quad (2)$$

where $\nu = \delta G / Y_0 \ll 1$ (see Appendix A2 for detailed derivations of the output coefficients). From Eq. (2), it is clear that in the small perturbation regime, the sensitivity may be boosted by an augment factor, $1/(\delta x)^2$. As ν increases, the output coefficient would rapidly converge to $\max(\Theta_{PT}) = 3+2\sqrt{2}$. Here, we also examine the sensor based on a Fabry-Perot (FP) resonator formed by a pair of lumped elements with conductance values $G = \sqrt{2}Y_0$, separated from each other by an electrical length $x = \pi + \delta x$. When $\psi_b^+/\psi_f^- = -1$, the FP resonator behaves like a CPA. Under small conductive perturbation, the output coefficient of the FP-type sensor is given by:

$$\Theta_{\mathrm{Fabry-Perot}} \approx \left(3-2\sqrt{2}\right)^2(1+2\nu^2)+\mathrm{O}(\nu^3). \quad (3)$$

Comparing Eqs. (2) and (3), we find that sensors based on the CPAL-locked electronic *PT* dimer can outperform the one based on the conventional FP resonator, in terms of sensitivity and modulation depth, thanks to the augment factor $1/(\delta x)^2$ that sharpens the derivative of $\Theta_{PT}(\nu)$. Such an effect can be clearly observed in Figs. 2(b) and 2(c), which present contours of Θ as a function of ν and δx for the CPAL-locked sensor and the FP-type sensor.

In the same vein, under small reactive perturbation ($i\delta B$), the output coefficient of the CPAL-locked sensor and the FP-type sensor can be approximately expressed as:

$$\Theta_{PT} \approx \frac{1}{4}\left[(\delta x)^2 + \frac{\mu^2}{(\delta x)^2} \right] + \mathrm{O}(\mu^3); \tag{4a}$$

$$\Theta_{\mathrm{Fabry-Perot}} \approx \left(3 - 2\sqrt{2}\right)^2 + (17\sqrt{2} - 24)\mu^2 + \mathrm{O}(\mu^3), \tag{4b}$$

where $\mu = \delta B / Y_0 \ll 1$. Again, it is evident from Eq. 4(a) that the sensitivity related to the first derivative of $\Theta_{PT}(\mu)$ can be enhanced by a factor of $1/(\delta x)^2$. Such an enhancement of sensitivity is, however, not obtained in the FP-type sensors.

In this work, we have built a laboratory prototype of the CPAL-locked electronic circuit on the printed circuit board (PCB). The schematics and the photograph of the PCB are shown in Figs. 1 (b) and 1(c). In our design, positive and negative shunt conductances are realized with a resistor and an NIC based on the feedback structure and a high-speed operational amplifier (OPA355). At 13.48 MHz, the effective impedance of the NIC and the resistor were measured to be $-35.56 - 0.18i$ [Ω] and 35.4 [Ω], respectively; here, we adopt the $e^{i\omega t}$ notation. The equivalent impedance and electrical length of the T-equivalent network are Y_0 and $x = \pi/2 + \delta x$, where $\delta x \sim 3\pi/40$. The PCB is connected to a two-port vector network analyzer with input conductance Y_0 = 1/50 S. This setup allows the system to operate near the CPAL point obtained when $G = |-G| = \sqrt{2}Y_0$ and $x = \pi/2$. In order to generate the conductive (reactive) perturbation to mimic a sensor or actuator with variable effective resistance (capacitance) [13,17–20], a shunt resistor (capacitor) of admittance δG ($i\delta B$) was added to the onboard *PT*-symmetric circuit; see Appendix A3 for the detailed implementation and measurement. Figure 2(a) compares the measured and simulated eigenvalues of the CPAL-locked circuit, showing a good agreement between both results near the CPAL point. In our simulation, the circuit simulation was performed using the Advanced Design System (ADS), with a realistic operational amplifier

mode [47,48]. In addition, the parasitic capacitance C_p and the parasitic resistance R_p existing in inductors L_1, L_2 and NIC were added in the *PT* circuit, as can be seen in Fig. 1(b).

Figures 3(a) and 3(b) present the measured *S*-parameters for the *PT* circuit in Fig. 1(c) under the conductive and reactive perturbation, respectively; here, the effect of C_p and R_p is already taken into consideration. It can be seen from Fig. 3 that the measurement (points) and simulation results (dashed lines) are in a good agreement. Without loss of generality, the output coefficients can be obtained from the measured *S*-parameters (see Appendix A3 for details). For a comparison, the RF FP resonator sketched in the inset of Fig. 4 was fabricated and measured. The electronic FP resonator is formed by a pair of resistors with $R = 35.4\,[\Omega]$ and a T-equivalent network with $x \approx \pi$. Figures 4(a) and 4(b) respectively depict the output coefficients Θ_{PT} and $\Theta_{\text{Fabry}-\text{Perot}}$ under conductive and reactive perturbations (i.e., by loading the circuit with different shunt resistors and capacitors); for each data point, the measurement was repeated by eight times for plotting the root-mean-square error (RMSE). The measurement and simulation results are in a good agreement, showing that the slope of output coefficient curve of the CPAL-locked circuit is remarkably larger than that of the FP-type circuit. As a result, the CPAL-locked RF sensor may be capable of detecting small conductive and reactive perturbations, well beyond the limitation of current passive RF sensor. We note that there exists slight discrepancies between the measured and simulated output coefficients, which could be attributed to fabrication errors and the parasitics of lumped elements mounted on the PCB, such as C_p, R_p, board defects, SMA connector flaws, and others. In practice, the above issues can be mitigated by using the complimentary metal-oxide-semiconductor (CMOS) and integrated circuit (IC) technologies. For on-chip NIC modulus (e.g., a cross-coupled pair or XCP that is commonly used in analog and RF ICs) and sensors, parasitic

elements could be partially or fully removed, and, therefore, the RMSE can be further minimized. Besides, through the on-chip techniques, the intentional phase offset (δx) of an equivalent network can be precisely controlled. As a result, on-chip techniques may allow one to push the sensitivity and detection limits of the CPAL-locked *PT*-symmetric sensor. To practically implement the proposed sensor initially locked at the CPA state, a high-resolution tunable phase shifter, such as those made of CMOS or microelectromechanical systems (MEMS) technologies, and an attenuator are required at a terminal of this RF circuit. The proposed CPAL sensor may be beneficial for various sensing scenarios. For example, in RF biosensing applications [49], a trapped living cell generally changes the reflection or transmission coefficient of a transmission line segment by less than 0.5 dB. However, the same cell, if regarded as a chemi-resistance perturbation, could lead to a tens of dB changes in the output coefficient of the CPAL sensor, which implies much improved sensitivity, detectability, and noise immunity.

Finally, we should note that the proposed CPAL-locked *PT*-symmetric sensor with the equivalent transmission line model sketched in Fig. 1(a) can also be implemented in the optical domain, where the gain and loss elements could be realized with the active and passive metasurfaces [24,38] and the phase offset is determined by the thickness of dielectric spacer or air gap.

To sum up, we have experimentally demonstrated a CPAL-locked *PT*-symmetric electronic circuitry that can be exploited to build monotonic RF sensors capable of detecting subtle impedance changes with high sensitivity. At the CPAL point, a small conductive or reactive disturbance in the sensing/actuation element can result in substantial changes in the output intensity. Our measurement results show that the proposed sensor can detect conductive and capacitive perturbations of the order of 10^{-2}, not possible with passive RF sensor based on a classical Fabry-Perot resonator. With further development and optimization of the electronic *PT* system using the CMOS

and/or on-chip MEMS technologies, the CPAL-based sensing mechanism can be exploited to build the next-generation ultrasensitive RF and microwave sensors and can be readily extended to interferometric optical sensors based on monotonic lights.

PYC would like to thank NSF ECCS-1711409 Grant for supporting this work.

APPENDIX A1: Scattering Properties and the CPAL Condition of the *PT* Circuit

The scattering matrix **S** of the *PT*-symmetric two-port transmission-line network in Fig. 1(a), with $G=\sqrt{2}Y_0$ and $-G=-\sqrt{2}Y_0$, can be derived as:

$$\mathbf{S}=\begin{pmatrix} \sec(x) & i\left(1+\sqrt{2}\right)\tan(x) \\ i\left(1-\sqrt{2}\right)\tan(x) & \sec(x) \end{pmatrix}. \tag{A1}$$

The CPAL point occurs when $x=\pi/2$. Throughout this study, we adopt the $e^{i\omega t}$ notation. The eigenvalues of **S** can be written as:

$$\lambda_{\pm}=\sec\left(\frac{\pi\omega}{2\omega_0}\right)\pm\tan\left(\frac{\pi\omega}{2\omega_0}\right), \tag{A2}$$

where ω is the angular frequency and ω_0 is the angular design frequency (frequency at CPAL point).

APPENDIX A2: Response of the Output Coefficient to Impedance Perturbations

When a conductive perturbation $\nu=\delta G/Y_0$ is applied to the *PT* circuit in Fig. 1(b) initially operating in the CPA mode (i.e., $\psi_b^+/\psi_f^-=i(\sqrt{2}-1)$), the output coefficient in response to ν can be derived as:

$$\Theta_{PT} = \frac{2\sqrt{2}\nu\left(\sec(\delta x)-1\right)-4\left(\sec(\delta x)-1\right)^2-\nu^2\sec^2(\delta x)}{(2\sqrt{2}-3)\nu^2-(\nu+2)^2\tan^2(\delta x)}$$
$$\approx \frac{1}{4}\left[(\delta x)^2+\frac{\nu^2}{(\delta x)^2}-\frac{(8-3\sqrt{2})}{4}\frac{\nu^3}{(\delta x)^2}+\mathrm{O}(\nu^4)\right], \quad \text{if} \quad \nu \ll 1 \tag{A3}$$
$$\approx \frac{1}{4}\left[(\delta x)^2+\frac{\nu^2}{(\delta x)^2}\right]+\mathrm{O}(\nu^3).$$

Similarly, the output coefficient as a function of ν for a Fabry-Perot CPA with $\psi_b^+/\psi_f^- = -1$ can be derived as:

$$\Theta_{\text{Fabry-Perot}} = \frac{\csc(\delta x)\left(\begin{array}{l}4i\left(2+\sqrt{2}\nu\right)-2i\left(4\sqrt{2}+\nu\left(6+\sqrt{2}\nu\right)\right)\cos(\delta x)\\ +4\left(2\sqrt{2}+\nu\right)\cot(\delta x)\\ +\left(-6+\nu^2-2\left(3+2\sqrt{2}\nu+\nu^2\right)\cos(\delta x)\right)\csc(\delta x)\end{array}\right)}{\left(4+2\sqrt{2}+\nu+\sqrt{2}\nu-\mathrm{i}\left(2+2\sqrt{2}+\nu\right)\cot(\delta x)\right)^2}$$
$$\approx \left(\frac{2(\sqrt{2}-1)+\nu}{2(\sqrt{2}+1)+\nu}\right)^2, \quad \text{if} \quad \nu \ll 1 \tag{A4}$$
$$\approx \left(3-2\sqrt{2}\right)^2(1+2\nu^2)+\mathrm{O}(\nu^3).$$

When the reactive perturbation $(\mu = \delta B/Y_0)$ is considered, the output coefficients of CPAL-locked *PT* circuit (initially set to the CPA mode) and the Fabry-Perot CPA are given by:

$$\Theta_{PT} = \frac{4-\sec(\delta x)\left(8-(\mu^2+4)\sec(\delta x)\right)}{(2\sqrt{2}-3)\mu^2-4(\sqrt{2}-1)\mu\tan(\delta x)+(\mu^2+4)\tan^2(\delta x)}$$
$$\approx \frac{1}{4}\left[(\delta x)^2+\frac{\mu^2}{(\delta x)^2}\right]+\mathrm{O}(\mu^3), \quad \text{if} \quad \mu \ll 1, \tag{A5}$$

and

$$\Theta_{\text{Fabry-Perot}} = \frac{\left[\begin{pmatrix} 2\left(5+2\sqrt{2}\mu+\mu^2\right)-4\left(2\sqrt{2}+\mu\right)\cos(\delta x) \\ -\left(-2+\mu^2\right)\cos(2\delta x) \end{pmatrix}\csc(\delta x)^2\right]}{\left[\begin{pmatrix} 4\left(3+2\sqrt{2}\right)\left(2+\cot(\delta x)^2\right)+\mu^2\left(3+2\sqrt{2}+\cot(\delta x)^2\right) \\ +4\mu\left(4+3\sqrt{2}+\left(1+\sqrt{2}\right)\cot^2(\delta x)\right) \end{pmatrix}\right]}$$

$$\approx \left(\frac{\sqrt{2}-1}{\sqrt{2}+1}\right)^2 + \frac{\sqrt{2}\mu^2}{(\sqrt{2}+1)^4} + \frac{2\sqrt{2}\mu}{(\sqrt{2}+1)^4}\delta x + \mathrm{O}(\mu^3), \quad \text{if} \quad \mu \ll 1 \tag{A6}$$

$$\approx \left(3-2\sqrt{2}\right)^2 + (17\sqrt{2}-24)\mu^2 + \mathrm{O}(\mu^3).$$

The CPA-like phenomena can be observed in a passive FP resonator when $\psi_b^+ / \psi_f^- = -1$, for which the eigenvalues are zero and unitary at the CPA point.

APPENDIX A3: Implementation and Measurement of the Onboard CPAL-Locked RF Sensor

In electronics, negative resistance can be obtained from an active negative-impedance converter (NIC) sketched schematically in Fig. 1(b), whose effective negative resistance is given by:

$$-R = -R_3 \frac{R_1}{R_2}, \tag{A7}$$

where R_1, R_2 and R_3 are labeled in Fig. 1(b) and an ideal operational amplifier with infinite open-loop gain is assumed. In our design, R_1 and R_2 were chosen to be $500\ [\Omega]$, R_3 was given by an adjustable trimmer potentiometer with maximum resistance of $100\ [\Omega]$, and a commercial operational amplifier (OPA355) was used to form a feedback loop, as shown in Fig. 1(b). Figure 5(a) plots the measured effective (shunt) impedance of this NIC. At the operating frequency ($\omega_0 = 13.48\,\mathrm{MHz}$), the effective impedance is $-35.56-0.18i\ [\Omega]$, which is quite close to the target value of $-25\sqrt{2}\ [\Omega]$. For saving the device area, a transmission line segment with characteristic impedance of $50\ [\Omega]$ and electrical length of x at the design frequency ω_0 can be

replaced by the T-equivalent network formed by two series inductors and a shunt capacitors [see Fig. 1(b)], which are:

$$C_1 = \frac{Y_0}{\omega_0 \sin(x)}, \text{ and } L_1 = L_2 = \frac{\sin(x)}{Y_0 \omega_0 (1-\cos(x))}. \quad \text{(A8)}$$

To observe the CPAL effect at 13.48 MHz, $C_1 = 236.1\ \text{pF} \approx 236\ \text{pF}$ and $L_1 = L_2 = 590.3\ \text{nH} \approx 590\ \text{nH}$ were chosen; here, 220 pF and 16 pF capacitors were connected in parallel to achieve the desired capacitance value, while 470 nH and 120 nH inductors were connected in series to achieve the required inductance. Besides, the inductors have a total intrinsic resistance of $5\ [\Omega]$ (R_p). Figure 5(b) presents the measured and simulated electrical length of this T-equivalent network, showing an electrical length $x = -88^{\circ}$ at the operating frequency and a phase offset $\delta x = -2^{\circ}$ or $-\pi/90$. We notice that fabrication tolerance of lumped elements and interconnection lines, as well as parasitics in NIC and SMA connectors contributed partially to the phase offset. Thus, when the equivalent network was integrated with the gain and loss elements, the phase offset was extracted to be $\delta x \sim 3\pi/40$. In order to mimic the resistive perturbation in a sensing or actuation element, a shunt resistor ($R = 1/\delta G$) or a shunt capacitor ($C = \delta G/\omega_0$) was added to the *PT*-symmetric pseudo sensing circuit. The output coefficient of the two-port *PT*-symmetric circuit can be expressed as:

$$\Theta = \frac{|\psi_b^-|^2 + |\psi_f^+|^2}{|\psi_f^-|^2 + |\psi_b^+|^2} = \frac{\left|1+\alpha(S_{12}/S_{11})\right|^2 + \left|\alpha + S_{21}/S_{11}\right|^2}{\left(1+|\alpha|^2\right)|1/S_{11}|^2}, \quad \text{(A9)}$$

where $\alpha = \psi_b^+/\psi_f^-$ and *S*-parameters can be found in Appendix A1. Without loss of generality, the output coefficients reported in Figs. 4(a) and (b) were obtained by substituting the measured *S*-parameters [Fig. 3] into Eq. (A9) and assuming $\alpha = i(\sqrt{2}-1)$. The S-matrix was characterized using the two-ports vector network analyzer (VNA).

REFERENCES

[1] C. M. Bender and S. Boettcher, *Real Spectra in Non-Hermitian Hamiltonians Having PT Symmetry*, Phys. Rev. Lett. **80**, 5243 (1998).

[2] R. El-Ganainy, K. G. Makris, M. Khajavikhan, Z. H. Musslimani, S. Rotter, and D. N. Christodoulides, *Non-Hermitian Physics and PT Symmetry*, Nature Phys **14**, 11 (2018).

[3] C. E. Rüter, K. G. Makris, R. El-Ganainy, D. N. Christodoulides, M. Segev, and D. Kip, *Observation of Parity–Time Symmetry in Optics*, Nature Phys **6**, 192 (2010).

[4] H. Ramezani, T. Kottos, R. El-Ganainy, and D. N. Christodoulides, *Unidirectional Nonlinear PT-Symmetric Optical Structures*, Phys. Rev. A **82**, 043803 (2010).

[5] R. El-Ganainy, K. G. Makris, D. N. Christodoulides, and Z. H. Musslimani, *Theory of Coupled Optical PT-Symmetric Structures*, Opt. Lett. **32**, 2632 (2007).

[6] Y. D. Chong, L. Ge, and A. D. Stone, *PT-Symmetry Breaking and Laser-Absorber Modes in Optical Scattering Systems*, Phys. Rev. Lett. **106**, 093902 (2011).

[7] Ş. K. Özdemir, S. Rotter, F. Nori, and L. Yang, *Parity-Time Symmetry and Exceptional Points in Photonics*, Nat. Mater. **18**, 783 (2019).

[8] M.-A. Miri and A. Alù, *Exceptional Points in Optics and Photonics*, Science **363**, eaar7709 (2019).

[9] A. Guo, G. J. Salamo, D. Duchesne, R. Morandotti, M. Volatier-Ravat, V. Aimez, G. A. Siviloglou, and D. N. Christodoulides, *Observation of PT-Symmetry Breaking in Complex Optical Potentials*, Phys. Rev. Lett. **103**, 093902 (2009).

[10] R. Fleury, D. Sounas, and A. Alù, *An Invisible Acoustic Sensor Based on Parity-Time Symmetry*, Nat Commun **6**, 5905 (2015).

[11] X. Zhu, H. Ramezani, C. Shi, J. Zhu, and X. Zhang, *PT-Symmetric Acoustics*, Phys. Rev. X **4**, 031042 (2014).

[12] J. Schindler, Z. Lin, J. M. Lee, H. Ramezani, F. M. Ellis, and T. Kottos, *PT-Symmetric Electronics*, J. Phys. A: Math. Theor. **45**, 444029 (2012).

[13] J. Schindler, A. Li, M. C. Zheng, F. M. Ellis, and T. Kottos, *Experimental Study of Active LRC Circuits with PT Symmetries*, Phys. Rev. A **84**, 040101 (2011).

[14] Y. Ra'di, D. L. Sounas, A. Alù, and S. A. Tretyakov, *Parity-Time-Symmetric Teleportation*, Phys. Rev. B **93**, 235427 (2016).

[15] J. M. Lee, S. Factor, Z. Lin, I. Vitebskiy, F. M. Ellis, and T. Kottos, *Reconfigurable Directional Lasing Modes in Cavities with Generalized PT Symmetry*, Phys. Rev. Lett. **112**, 253902 (2014).

[16] Z. Ye, M. Farhat, and P.-Y. Chen, *Tunability and Switching of Fano and Lorentz Resonances in PTX-Symmetric Electronic Systems*, Appl. Phys. Lett. **117**, 031101 (2020).

[17] P.-Y. Chen, M. Sakhdari, M. Hajizadegan, Q. Cui, M. M.-C. Cheng, R. El-Ganainy, and A. Alù, *Generalized Parity–Time Symmetry Condition for Enhanced Sensor Telemetry*, Nat Electron **1**, 297 (2018).

[18] M. Sakhdari, M. Hajizadegan, Q. Zhong, D. N. Christodoulides, R. El-Ganainy, and P.-Y. Chen, *Experimental Observation of PT Symmetry Breaking near Divergent Exceptional Points*, Phys. Rev. Lett. **123**, 193901 (2019).

[19] Z. Dong, Z. Li, F. Yang, C.-W. Qiu, and J. S. Ho, *Sensitive Readout of Implantable Microsensors Using a Wireless System Locked to an Exceptional Point*, Nat Electron **2**, 335 (2019).

[20] M. Sakhdari, M. Hajizadegan, Y. Li, M. M.-C. Cheng, J. C. H. Hung, and P.-Y. Chen, *Ultrasensitive, Parity–Time-Symmetric Wireless Reactive and Resistive Sensors*, IEEE Sensors Journal **18**, 9548 (2018).

[21] M. C. Rechtsman, *Optical Sensing Gets Exceptional*, Nature **548**, 161 (2017).

[22] W. Chen, Ş. Kaya Özdemir, G. Zhao, J. Wiersig, and L. Yang, *Exceptional Points Enhance Sensing in an Optical Microcavity*, Nature **548**, 192 (2017).

[23] P.-Y. Chen and R. El-Ganainy, *Exceptional Points Enhance Wireless Readout*, Nat Electron **2**, 323 (2019).

[24] P.-Y. Chen and J. Jung, *PT Symmetry and Singularity-Enhanced Sensing Based on Photoexcited Graphene Metasurfaces*, Phys. Rev. Applied **5**, 064018 (2016).

[25] M. Hajizadegan, M. Sakhdari, S. Liao, and P.-Y. Chen, *High-Sensitivity Wireless Displacement Sensing Enabled by PT-Symmetric Telemetry*, IEEE Transactions on Antennas and Propagation **67**, 3445 (2019).

[26] R. Fleury, D. L. Sounas, and A. Alù, *Negative Refraction and Planar Focusing Based on Parity-Time Symmetric Metasurfaces*, Phys. Rev. Lett. **113**, 023903 (2014).

[27] X. Lin, Y. Yang, N. Rivera, J. J. López, Y. Shen, I. Kaminer, H. Chen, B. Zhang, J. D. Joannopoulos, and M. Soljačić, *All-Angle Negative Refraction of Highly Squeezed Plasmon and Phonon Polaritons in Graphene–Boron Nitride Heterostructures*, Proc Natl Acad Sci USA 201701830 (2017).

[28] Z. Lin, H. Ramezani, T. Eichelkraut, T. Kottos, H. Cao, and D. N. Christodoulides, *Unidirectional Invisibility Induced by PT-Symmetric Periodic Structures*, Phys. Rev. Lett. **106**, 213901 (2011).

[29] L. Chang, X. Jiang, S. Hua, C. Yang, J. Wen, L. Jiang, G. Li, G. Wang, and M. Xiao, *Parity–Time Symmetry and Variable Optical Isolation in Active–Passive-Coupled Microresonators*, Nature Photon **8**, 524 (2014).

[30] L. Feng, Y.-L. Xu, W. S. Fegadolli, M.-H. Lu, J. E. B. Oliveira, V. R. Almeida, Y.-F. Chen, and A. Scherer, *Experimental Demonstration of a Unidirectional Reflectionless Parity-Time Metamaterial at Optical Frequencies*, Nature Mater **12**, 108 (2013).

[31] S. Savoia, G. Castaldi, V. Galdi, A. Alù, and N. Engheta, *Tunneling of Obliquely Incident Waves through PT-Symmetric Epsilon-near-Zero Bilayers*, Phys. Rev. B **89**, 085105 (2014).

[32] J. Doppler, A. A. Mailybaev, J. Böhm, U. Kuhl, A. Girschik, F. Libisch, T. J. Milburn, P. Rabl, N. Moiseyev, and S. Rotter, *Dynamically Encircling an Exceptional Point for Asymmetric Mode Switching*, Nature **537**, 76 (2016).

[33] S. Savoia, G. Castaldi, and V. Galdi, *Non-Hermiticity-Induced Wave Confinement and Guiding in Loss-Gain-Loss Three-Layer Systems*, Phys. Rev. A **94**, 043838 (2016).

[34] D. L. Sounas, R. Fleury, and A. Alù, *Unidirectional Cloaking Based on Metasurfaces with Balanced Loss and Gain*, Phys. Rev. Applied **4**, 014005 (2015).

[35] S. Assawaworrarit, X. Yu, and S. Fan, *Robust Wireless Power Transfer Using a Nonlinear Parity–Time-Symmetric Circuit*, Nature **546**, 387 (2017).

[36] M. Sakhdari, M. Hajizadegan, and P.-Y. Chen, *Robust Extended-Range Wireless Power Transfer Using a Higher-Order PT-Symmetric Platform*, Phys. Rev. Research **2**, 013152 (2020).

[37] S. Longhi, *PT -Symmetric Laser Absorber*, Phys. Rev. A **82**, 031801 (2010).

[38] M. Sakhdari, N. M. Estakhri, H. Bagci, and P.-Y. Chen, *Low-Threshold Lasing and Coherent Perfect Absorption in Generalized P T -Symmetric Optical Structures*, Phys. Rev. Applied **10**, 024030 (2018).

[39] Z. J. Wong, Y.-L. Xu, J. Kim, K. O'Brien, Y. Wang, L. Feng, and X. Zhang, *Lasing and Anti-Lasing in a Single Cavity*, Nature Photon **10**, 796 (2016).

[40] L. Feng, Z. J. Wong, R.-M. Ma, Y. Wang, and X. Zhang, *Single-Mode Laser by Parity-Time Symmetry Breaking*, Science **346**, 972 (2014).

[41] H. Hodaei, M.-A. Miri, M. Heinrich, D. N. Christodoulides, and M. Khajavikhan, *Parity-Time-Symmetric Microring Lasers*, Science **346**, 975 (2014).

[42] Y. Sun, W. Tan, H. Li, J. Li, and H. Chen, *Experimental Demonstration of a Coherent Perfect Absorber with PT Phase Transition*, Phys. Rev. Lett. **112**, 143903 (2014).

[43] Z. Xiao, H. Li, T. Kottos, and A. Alù, *Enhanced Sensing and Nondegraded Thermal Noise Performance Based on PT-Symmetric Electronic Circuits with a Sixth-Order Exceptional Point*, Phys. Rev. Lett. **123**, 213901 (2019).

[44] N. A. Mortensen, P. A. D. Gonçalves, M. Khajavikhan, D. N. Christodoulides, C. Tserkezis, and C. Wolff, *Fluctuations and Noise-Limited Sensing near the Exceptional Point of Parity-Time-Symmetric Resonator Systems*, Optica **5**, 1342 (2018).

[45] W. Langbein, *No Exceptional Precision of Exceptional-Point Sensors*, Phys. Rev. A **98**, 023805 (2018).

[46] M. Farhat, M. Yang, Z. Ye, and P.-Y. Chen, *PT-Symmetric Absorber-Laser Enables Electromagnetic Sensors with Unprecedented Sensitivity*, ACS Photonics **7**, 2080 (2020).

[47] Keysight, *PathWave Advanced Design System (ADS)*, https://www.keysight.com/us/en/products/software/pathwave-design-software/pathwave-advanced-design-system.html.

[48] *OPA355 Data Sheet, Product Information and Support | TI.Com*, https://www.ti.com/product/OPA355.

[49] A. Paffi, M. Liberti, F. Apollonio, X. Ma, X. Du, and J. C. M. Hwang, *Modeling and Analysis for Ultra-Wideband Single-Cell Sensing by a Coplanar Waveguide*, in *2019 49th European Microwave Conference (EuMC)* (IEEE, Paris, France, 2019), pp. 89–92.

FIGURES

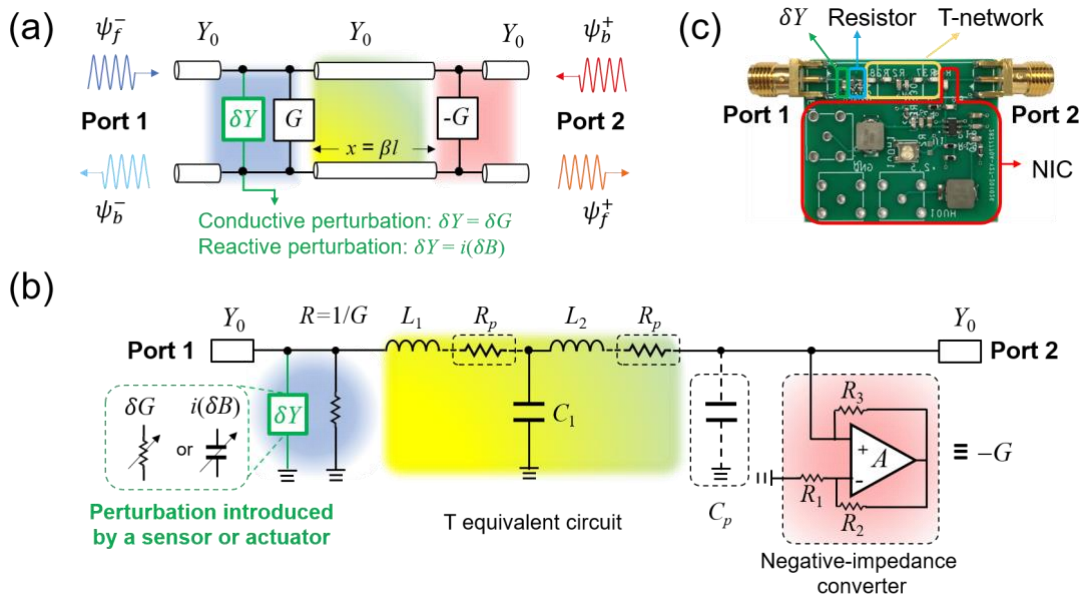

FIG. 1. (a) Equivalent transmission-line model for the generalized *PT*-symmetric system and (b) its practical realization in the RF range; here, a shunt resistor or capacitor of different values (i.e., pseudo-sensor) is used to mimic the impedance variations in a sensing/actuation element. (c) Photograph of the CPAL-locked *PT*-symmetric RF circuit in (b), realized with the printed-circuit board (PCB) technique.

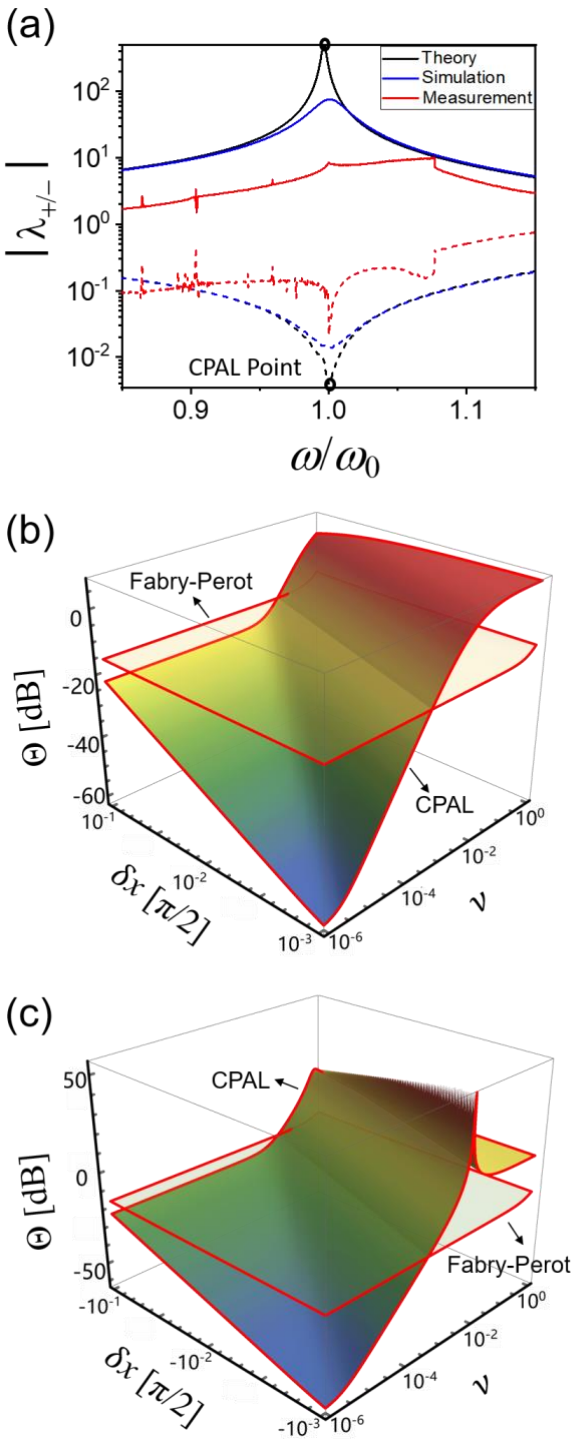

FIG. 2. (a) Evolution of the eigenvalues as a function of the normalized frequency for the *PT*-symmetric electronic circuit in Fig. 1; here, $G = |-G| = \sqrt{2}Y_0$ and $x(\omega_0) = 0.99\pi/2$. The measurement (red lines) and simulation results (blue lines) are in a good agreement at the CPAL point. Contours of the output coefficient as a function of conductive perturbation ν for the CPAL-locked *PT*-symmetric system in Fig. 1(a)

and a passive Fabry-Perot resonator, with the (b) positive phase offset δx, and (c) negative phase offset $-\delta x$.

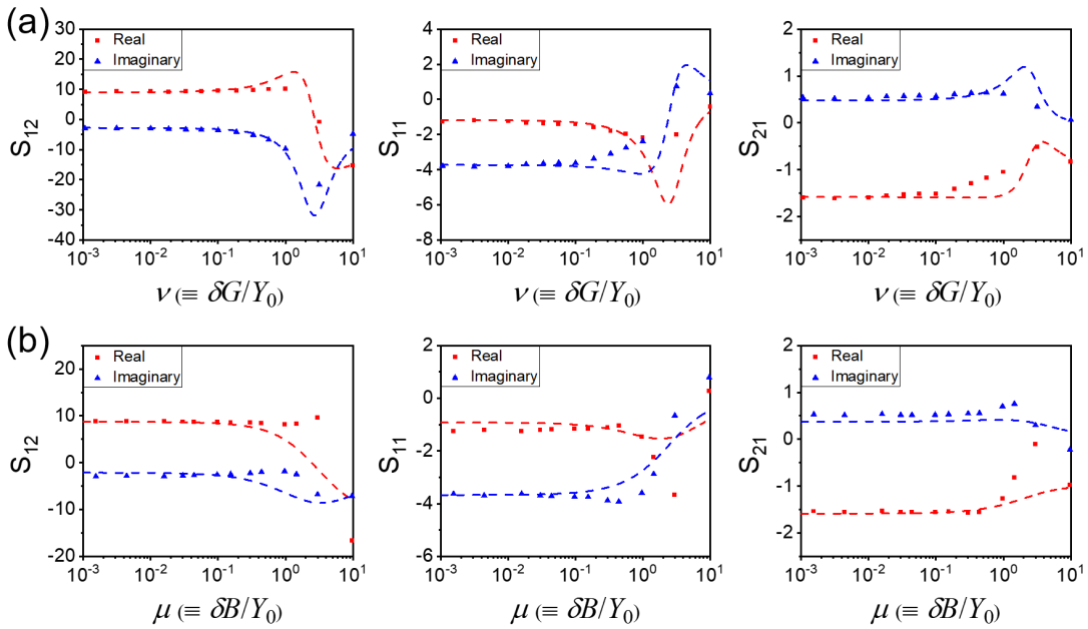

FIG. 3. Measured (points) and simulated (dashed lines) real (red) and imaginary (blue) parts of the *S*-parameters, under the (a) conductive and (b) reactive perturbation. For both cases, the simulation results agree well with the measured ones in the working range. The simulation was based on the equivalent circuit model in Fig. 1(b), with effective parasitic capacitance and realistic SPICE model for the operational amplifier.

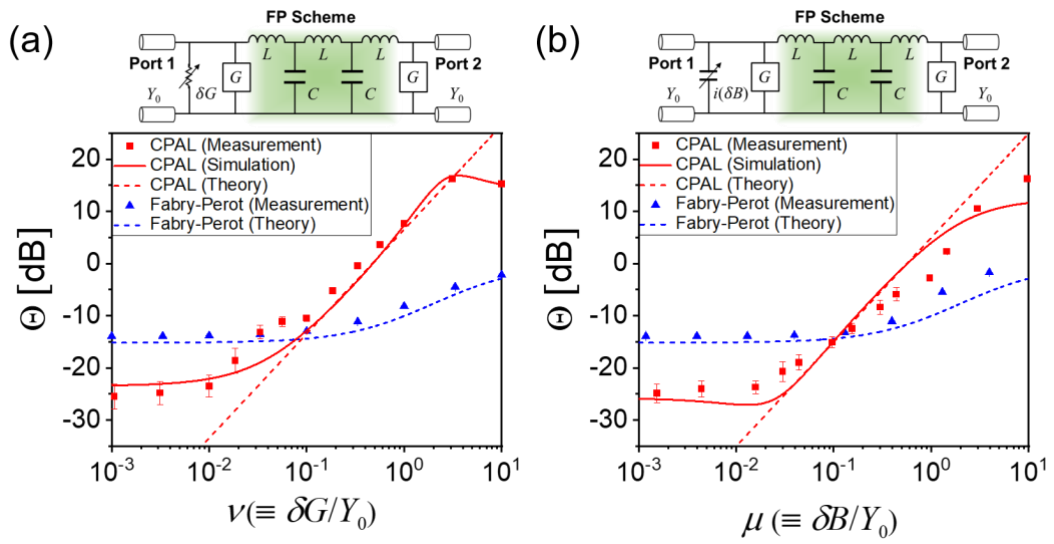

FIG. 4. (a) Output coefficient versus conductive perturbation $\nu = \delta G / Y_0$ for the CPAL-locked (red lines) and FP (blue lines) RF sensors sketched in the inset; here, the points, solid and dashed lines represent the measurement, simulation and theoretical results (according to Eqs. (2) and (3)), respectively. When plotting the theoretical predictions, the phase offset $\delta x = 3\pi / 40$ was used to fit the measurement results. The maximal error bar of CPAL sensor is below 2.4 dB. (c) is similar to (b), but for the reactive perturbation $\mu = i(\delta B) / Y_0$; here, the theoretical prediction is based on Eq. (4).

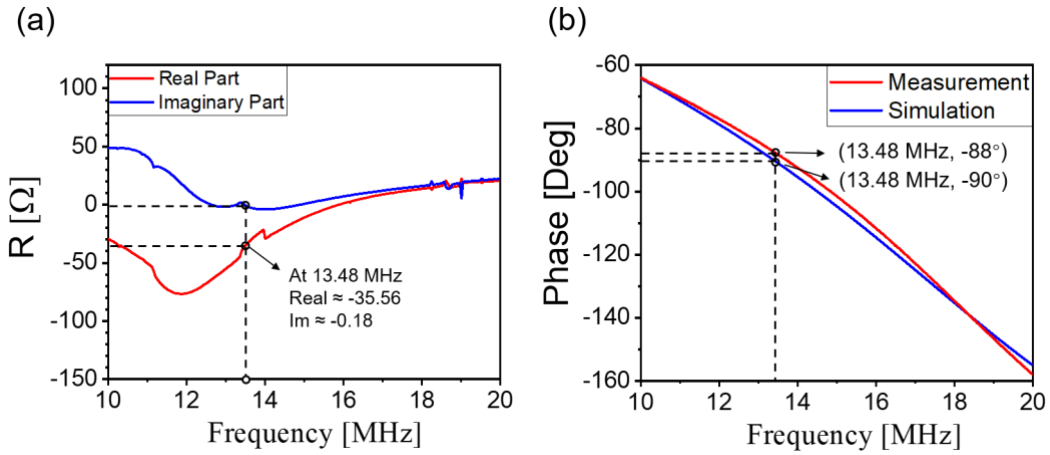

FIG. 5. (a) Real (red line) and imaginary (blue line) parts of the measured impedance of the NIC. At 13.48 MHz, the input impedance is $-35.56-0.18i$ [Ω], which is close to the value required for the CPAL condition ($-25\sqrt{2}$ [Ω].). (b) Measured (red line) and simulated (blue line) electrical length of the T-equivalent network. At the design frequency of 13.48 MHz, the measured electrical length is -88°.

Table of Content